The International Journal of Advanced Manufacturing Technology (2023) 125:2717–2731
https://doi.org/10.1007/s00170-023-10880-w

ORIGINAL ARTICLE

Five-axis flank milling error model of a face gear considering the tool tip dynamics

Sijie Cai[1] · Jianchun Liu[1] · Bin Yao[2] · Zhiqin Cai[2] · Zhihuang Shen[3] · Haipeng Huang[1] · Bingjing Lin[1] · Jianchun Lin[1] · Haibin Huang[1]

Received: 12 May 2022 / Accepted: 11 January 2023 / Published online: 25 January 2023

Abstract
The five-axis flank milling process of sculptured surfaces is an intricate process involving time-varying and nonlinear characteristics under the multiphysics coupling effect. The milling force during the process is an important factor that influences the machining accuracy of sculptured surfaces. Face gears, as parts with sculptured surfaces, are widely employed in the aerospace and machinery manufacturing industries. To realize the high-precision manufacturing of face gears with a universal milling machine, this study proposes a five-axis flank milling method for face gears. In addition, based on the tangent plane approximation algorithm and the Receptance Coupling Substructure Analysis (RCSA) method, the milling force and the tool tip vibration during the face gear machining process are investigated. Finally, a five-axis flank milling force model and a face gear surface machining error model are established considering the interaction between the milling force and the process system.

Keywords Sculptured surface · Face gear · Five-axis flank milling · Cutting force · Receptance Coupling Substructure Analysis · Tool tip frequency function

1 Introduction

Owing to the continuous improvement of the performance requirements for mechanical products, the manufacturing accuracy and surface quality requirements of many parts with sculptured surface, such as face gears and impellers, are also being enhanced continuously. In the process of sculptured surface machining, analyzing the impact of the physical behavior coupling effect of the cutter–workpiece contact position on the surface manufacturing accuracy is of great importance [1, 2]. The milling force excitation is a crucial factor underlying the vibration and deformation of the milling cutter. Hence, investigating the interaction between the milling force and the process system is the premise for accurate modeling of the milling force and the surface machining error.

The cutting force coefficient is a key factor that influences the milling force of the milling cutter. The first step for predicting the milling force is identifying the cutting force coefficient. The cutting force coefficient identification method based on the average cutting force is typically used in the milling force model [3, 4]. Ko et al. [5] proposed a cutting force coefficient identification method based on the transient cutting force to study the change in the cutting force coefficient in the milling process. Accordingly, Tuysuz et al. [6] proposed the deformed cutting force coefficient to investigate the influence of the workpiece deformation on the milling force during the cutting process. Another key factor that influences the milling force is the contact area. The ball-end milling process involves the highly complex cutter–workpiece contact area. Kim et al. [7] calculated the contact area, cut-in angle, and cut-out angle based on the Z-map method. Cao et al. [8] studied the influence of the cutter orientation on the shape of the cutter–workpiece contact area and simulated the milling force of the ball-end milling cutter. The undeformed chip thickness is the

✉ Sijie Cai
xmucsj@163.com

[1] School of Mechanical and Automotive Engineering, Jimei District, Xiamen University of Technology, Xiamen 361021, Fujian Province, China

[2] Department of Mechanical and Electrical Engineering, Xiamen University, Xiang'an District, Xiamen 361106, Fujian Province, China

[3] School of the Mechanical and Energy Engineering, Jimei District, Jimei University, Xiamen 361021, Fujian Province, China

most important parameter of the milling force model. To simulate the milling force in the multiaxis flank milling of end-milling cutters and round-nose cutters, Zhang et al. [9] integrated the microelement trajectory model of the cutting edge of the milling cutter and explored a method for modeling its undeformed chip thickness, cut-in angle, and cut-out angle. Rao [10] proposed a numerical calculation method to calculate the undeformed chip thickness and simulate the five-axis flank milling force.

Calculating the frequency response function of the tool tip is a key step toward establishing the coupled vibration milling force model. Yao et al. [11, 12] collected the modal parameters of the tool tip frequency response function using the modal parameter identification method, adopted the Runge–Kutta method to calculate the vibration curve, and established the dynamic milling force model of the coupled vibration plane. To study the dynamic characteristics of the joint surface of the cutter–tool holder–spindle system, Schmitz et al. proposed the flexible Receptance Coupling Substructure Analysis (RCSA) method [13] and the rigid RCSA method [14], established the cutter–tool holder–spindle system dynamics model by integrating the cutter finite element model [15], and extracted the dynamic parameters of the joint surface.

To predict the cutting force and the machining error accurately, the interaction of the cutting force and the machining system must be studied [16]. Cai et al. [17] proposed the pixel scanning method to calculate the undeformed chip thickness and simulated the cutting force and surface topography including the influence of the vibration. Altintas et al. [18] calculated the cutter–workpiece contact area and simulated the milling force based on the cutter orientation, and the machining error was predicted on the basis of the cutting force and the modal parameters of the tool tip. Li et al. [19] established the time-varying dynamics model of a thin-walled workpiece based on the life and death element method and predicted the milling force and the machining error of the thin-walled workpiece including the interaction of the cutting force and the machining system. Li et al. [20] measured the tool tip frequency function and calculated the undeformed chip thickness including the influence of the cutter vibration and simulated the milling force. Edouard and Filippi [21] calculated the chip thickness and predicted the cutting force under the condition of cutter runout considering the interaction of the cutting force and the machining system.

Few studies have investigated cutting force models and machining error models for the sculptured surface milling process considering the interaction between the cutting force and the vibration of the tool tip, especially for sculptured surface milling using a milling cutter with a small diameter. To realize high-precision manufacturing of face gears with a universal milling machine, this study integrates the five-axis flank milling method for machining the face gears and explores a method for establishing the physical behavior and the machining error model considering the cutter vibration during the milling process. The model of the undeformed chip thickness in the five-axis milling process is established using the tangent plane approximation algorithm and combined with the milling force coefficient to explore a method for modeling the five-axis milling force. It is difficult to directly measure the tool tip frequency response for a milling cutter spindle system with a small diameter. To address this problem, the tool tip frequency response function is predicted on the basis of the flexible RCSA method. Based on the aforementioned models, the cutting force model and the machining error model considering the interaction of the cutting force and the milling cutter can be established considering the tool path and the orientation of the face gear milling process. Because this algorithm simulates the milling process considering the interaction of the cutting force and the machining system, the machining error model can achieve higher precision [17].

1.1 Mechanical model of multiaxis flank milling of end-milling cutter

Based on the structure of the five-axis machine shown in Fig. 1a, the dynamic milling force in the process of flank milling of the sculptured surface with the end-milling cutter is investigated. The machining and workpiece coordinate systems are established. The coordinate origin of the workpiece coordinate system coincides with the center of the top of the face gear. The x, y, and z axes of the workpiece coordinate system are parallel to the X, Y, and Z axes of the machine cutter, respectively. The face gear and the workpiece coordinate system are relatively static. In the initial state of machining, the machining coordinate system coincides with the workpiece coordinate system. Let (X_n, Y_n, Z_n) be the coordinates of the n-th cutter location point in the workpiece coordinate system, and let B_n and C_n be the machine cutter B and C axis rotation angles corresponding to the n-th cutter location point. Figure 1b shows a schematic diagram of milling cutter path interpolation. The machine cutter motion axis performs linear interpolation between two cutter location points. The motion time of the cutter among the cutter location points is calculated according to the feed rate. Moreover, the relationship model between the cutter orientation and parameter t is established as follows:

$$\begin{cases} t_n = \dfrac{\sqrt{(x_n - x_{n-1})^2 + (y_n - y_{n-1})^2 + (z_n - z_{n-1})^2}}{f} + t_{n-1} \\ X(t) = X_n + \dfrac{t - t_{n-1}}{t_n - t_{n-1}}(X_n - X_{n-1}) \\ Y(t) = Y_n + \dfrac{t - t_{n-1}}{t_n - t_{n-1}}(Y_n - Y_{n-1}) \\ Z(t) = Z_n + \dfrac{t - t_{n-1}}{t_n - t_{n-1}}(Z_n - Z_{n-1}) \\ B(t) = B_n + \dfrac{t - t_{n-1}}{t_n - t_{n-1}}(B_n - B_{n-1}) \\ C(t) = C_n + \dfrac{t - t_{n-1}}{t_n - t_{n-1}}(C_n - C_{n-1}) \end{cases} \quad (1)$$

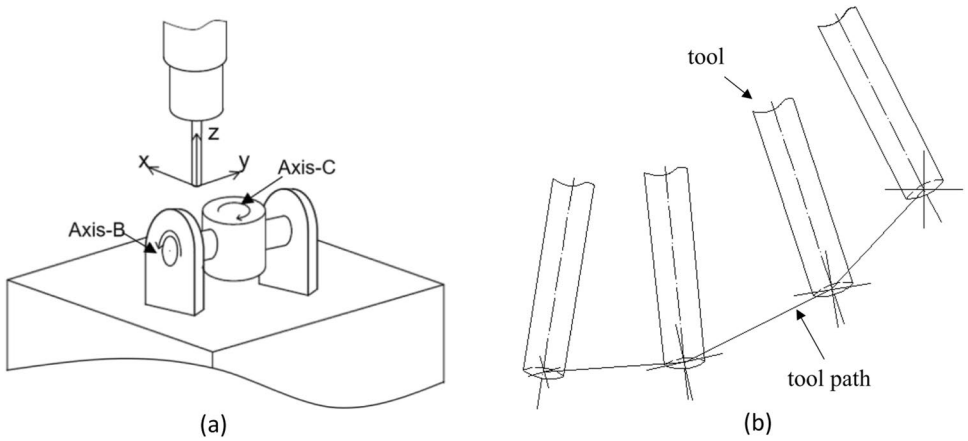

Fig. 1 Structure and the cutting path of the five-axis machine

where f is the feed rate; t_n is the total time for the cutter to move from the first cutter location point to the n-th cutter location point; and $(X(t), Y(t), Z(t), B(t), C(t))$ denote the cutter location point and the orientation of the cutter in the workpiece coordinate system at time t. Combined with the cutter location point and the orientation of the cutter axis, a cutter axis motion path model considering the influence of cutter vibration is established as follows:

$$S_c(t,a_p) = RotC(t)Rot(-B(t))\left(\begin{bmatrix} 0 \\ 0 \\ a_p \end{bmatrix} + \begin{bmatrix} x_v(t) \\ y_v(t) \\ z_v(t) \end{bmatrix}\right) + \begin{bmatrix} X(t) \\ Y(t) \\ Z(t) \end{bmatrix} \tag{2}$$

where $S_c(t,a_p)$ denotes the position and orientation of the cutter axis in the workpiece coordinate system at time t; $(x_v(t), y_v(t), z_v(t))$ denote the vibration amount of the cutter along the x, y, and z axes of the machining coordinate system, respectively, during the machining process; and a_p is the distance between the calculation point and the end face of the cutter along the cutter axis direction. The cutter–tool holder–spindle process system has strong axial rigidity and weak radial rigidity. In addition, the radial vibration of the cutter has a significant impact on the workpiece surface morphology, manufacturing error, and cutting force during the flank milling process. Hence, the axial vibration of the cutter $z_v(t)$ is ignored in the calculation process.

The cutting edge path model considering the influence of cutter vibration is calculated according to the cutter location point and the orientation of the cutter axis. The cutting edge path model is established as follows:

$$S_i(t,a_p) = \mathrm{Rot}C(t)\mathrm{Rot}(-B(t))\left(\begin{bmatrix} r\cos(wt+\varphi_0+\varphi_i+\frac{a_p\tan\beta_i}{r}) \\ r\cos(wt+\varphi_0+\varphi_i+\frac{a_p\tan\beta_i}{r}) \\ a_p \end{bmatrix} + \begin{bmatrix} x_v(t) \\ y_v(t) \\ z_v(t) \end{bmatrix}\right) + \begin{bmatrix} X(t) \\ Y(t) \\ Z(t) \end{bmatrix} \tag{3}$$

where r is the radius of the cutter; w is the rotational angular velocity of the cutter; φ_0 is the initial phase angle of the first cutting edge; φ_i is the face-tooth angle between the i-th cutting edge and the first cutting edge; β_i is the helix angle of the i-th cutting edge; $\mathbf{S_i}$ (t, a_p) is the motion path surface of the i-th cutting edge; $\mathbf{S_{i-1}}$ (t, a_p) is the motion path surface of the (i-1)-th cutting edge or the transition surface during the cutting process of the i-th cutting edge; t is the motion time of the cutter; and a_p is the distance between the cutting edge microelement and the end face of the cutter along the cutter axis. By integrating the microelement motion path model of the cutting edge and the transition surface model of the cutter cutting process, the undeformed chip thickness is calculated. The modeling method is shown in Fig. 2, where **CO** and **C′O′** are the cutter axis vectors at different times; **OO′** is the cutter path; B is the microelement position of the cutting edge currently participating in cutting; and BA is the undeformed chip thickness. The algorithm flow is shown in Fig. 3.

The equation for calculating the direction **CB** of the undeformed chip thickness is given by Eq. 4, where u is the equation parameter. The intersection of Eq. 4 and the transition surface $\mathbf{S_{i-1}}$ in the milling process is determined, where BA is the undeformed chip thickness. $\mathbf{S_{i-1}}$ can be represented by Eq. 3. As $\mathbf{S_{i-1}}$ is a nonlinear function, it is difficult to obtain the parameters t and a_p directly from simultaneous Eqs. 3 and 4. The undeformed chip thickness is calculated using the tangent plane approximation algorithm. First, an iterative initial point $\mathbf{A_0}$ is taken on the milling transition surface $\mathbf{S_{i-1}}$. The parameter t of point $\mathbf{A_0}$ and the parameter t of point **B** differ by one milling force cycle, and the parameter a_p of point $\mathbf{A_0}$ is the same as the parameter a_p of point **B**. Based on Taylor expansion, the tangent plane $\mathbf{A_0}$* of the transition surface at point $\mathbf{A_0}$ is obtained, and its mathematical model is expressed as follows:

$$S_c(t,a_p) + u\frac{S_i(t,a_p) - S_c(t,a_p)}{\left|S_i(t,a_p) - S_c(t,a_p)\right|} = 0 \tag{4}$$

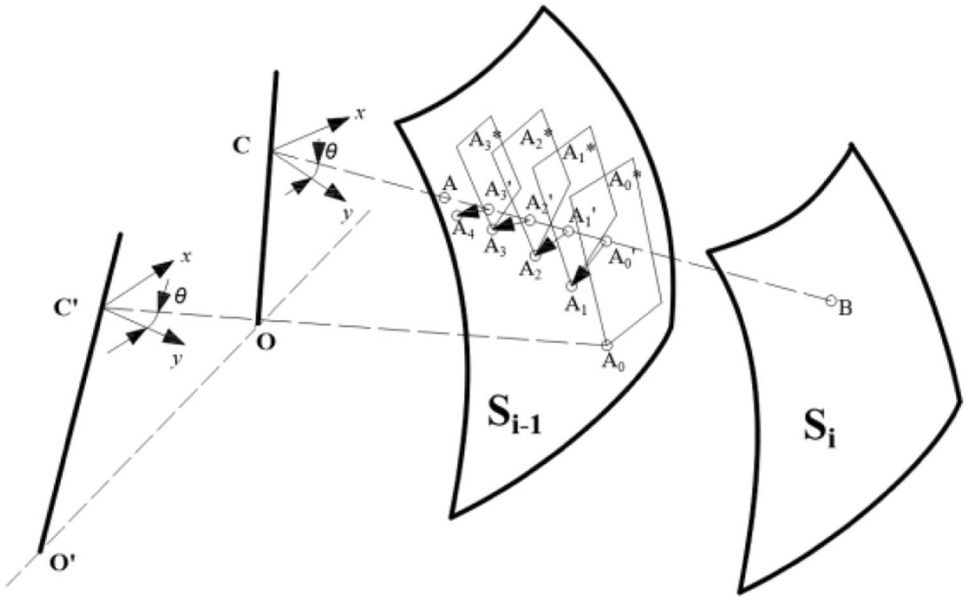

Fig. 2 Undeform chip thickness model

$$S_{i-1}^{*}(t,a_p)=S_{i-1}(t_k,a_{p,k})+\frac{\partial S_{i-1}}{\partial t_k}\Delta t+\frac{\partial S_{i-1}}{\partial a_{i-1,k}}\Delta a_p \tag{5}$$

where S_{i-1}^{*} is the mathematical expression of the tangent plane; Δt is the time difference; and Δa_p is the distance difference between the cutting edge microelement and the end face of the cutter. The tangent plane equation and the straight line equation are simultaneously established. As the simultaneous equation of the tangent plane equation and the straight line equation form a linear equation system, it is easy to obtain Δt and Δa_p. The parameter coordinates of the intersection point $\mathbf{A_0'}$ of the tangent plane and the straight line can be obtained through the parameter coordinates of the initial point $\mathbf{A_0}$. The parameter coordinates corresponding to the point $\mathbf{A_0'}$ can be substituted into Eq. 3 to obtain point $\mathbf{A_1}$ on the transition surface. The distance L_i between the point $\mathbf{A_1}$ and the point $\mathbf{B}$ is calculated. The tangent plane of the transition surface is continued to be generated at point $\mathbf{A_1}$. The aforementioned process for iterative calculation is repeated. The closer the point $\mathbf{A_k}$ obtained on the transition surface is to the intersection of the straight line and the transition surface, the closer is the distance L_k obtained at iteration step k to the distance L_{k-1} obtained at iteration step k-1. When the iterative calculation reaches the convergence condition given by Eq. 6, the iteration is terminated. At this time, L_k is the undeformed chip thickness and σ is the allowable iteration error.

$$\left|L_k-L_{k-1}\right|<\sigma \tag{6}$$

Based on the tangent plane approximation model, the cut-in and cut-out angle model [9] of the cutting process can be established. By integrating the cut-in angle and cut-out angle models, we can determine whether the cutting edge microelement participates in the cutting at a certain moment in the cutting process according to the rotation angle of the milling cutter. The milling force can be predicted by combining the average milling force coefficient identification method and the linear cutting edge microelement model [17].

1.2 Calculation of the tool tip frequency response function of a slender milling cutter

Based on the flexible RCSA method, the dynamic model of the cutter–tool holder–spindle system is established. The tool tip frequency response function of a slender milling cutter is calculated by combining the measured frequency response function and the finite element modeling method. The cutter–tool holder–spindle system model considering the dynamic parameters of the joint surface is shown in Fig. 4. This system can be divided into three substructures: cutter, tool holder, and spindle system. The spring-damping element is used to simulate the contact stiffness and damping of the joint surfaces between the substructures. To accurately calculate the tool tip frequency response function, it is necessary to first identify the dynamic parameter $\mathbf{K}$ of the joint surface. As the frequency response of the tool holder gripper position can be directly measured, this study investigates only the dynamic parameter matrix $\mathbf{K}$ of the cutter–cutter handle joint surface.

Figure 5 shows the flow of the calculation method of the tool tip frequency response function (FRF) of the slender milling cutter based on the RCSA method. The specific steps are as follows.

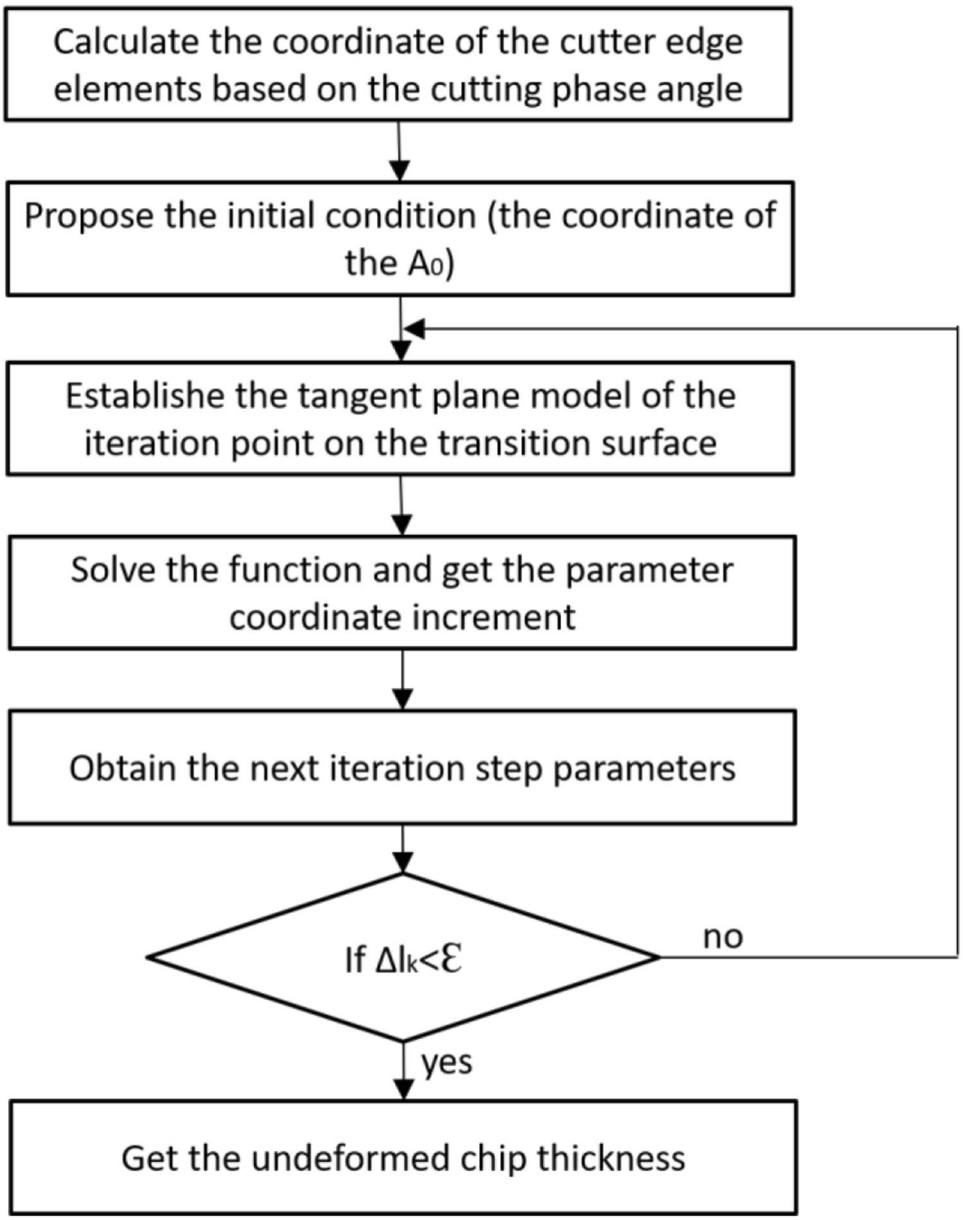

Fig. 3 Undeformed chip thickness algorithm

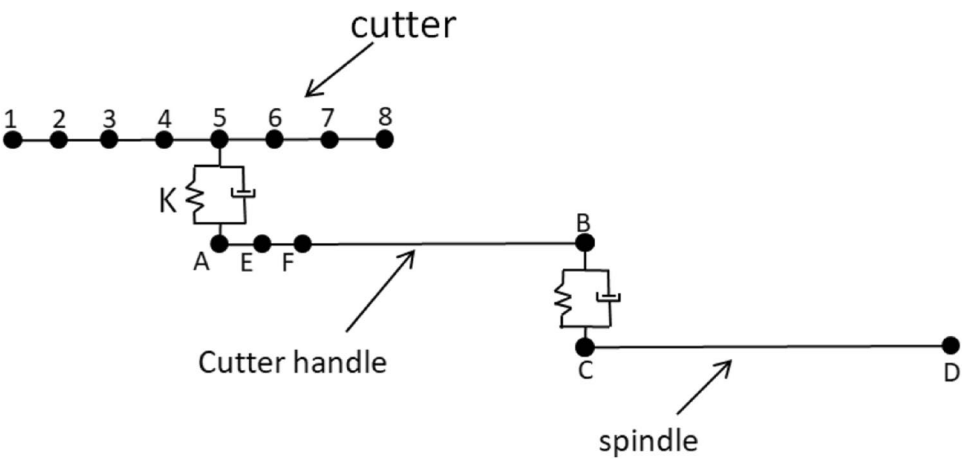

Fig. 4 Finite element model of the cutter–shank–spindle system

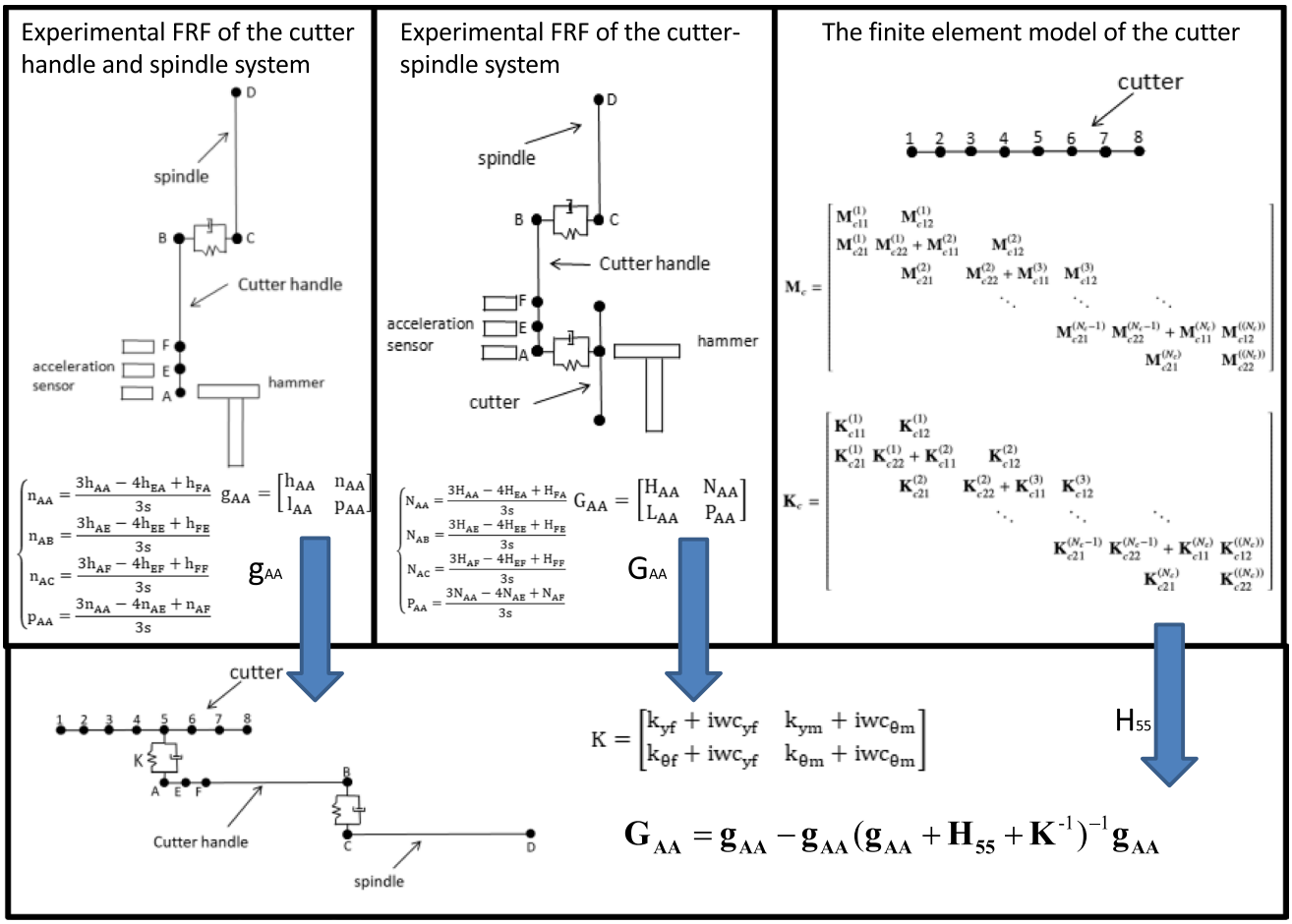

Fig. 5 Algorithm of the FRF of the slender cutter tool tip based on RCSA

Table 1 Parameters of the cutter finite element

Beam number	1	2	3	4	5	6	7
Diameter of the beam/mm	2	2	2	3	4	4	4
Length of the beam/mm	4	4	2	2	8	13	24

1. The tool tip frequency response function and the contact position frequency response function between the cutter and the tool holder in the free state of the cutter are calculated. Referring to the Timoshenko element model considering gravity, as reported by Yokomada [15], the cutter impedance matrix in the free state is calculated. The geometric parameters of each element in the cutter are listed in Table 1, and the material parameters of the cutter are summarized in Table 2. According to the cutter impedance matrix, the modal parameters and modal shape can be obtained through modal analysis. The frequency response function of each node can be calculated using the frequency response function model. It is assumed that the first node is the tool tip node and the fifth node is the cutter node at the contact position between the cutter and the tool holder. Then, the cutter frequency response $\mathbf{H_{11}}$, $\mathbf{H_{15}}$, $\mathbf{H_{51}}$, and $\mathbf{H_{55}}$ must be predicted. As the modeling method has been described previously, its details are omitted here.

Table 2 Parameters of the cutter material

Material	Elastic modulus (Pa)	Poisson's radio	Density (kg/m^3)	Damping coefficient
YG8	6.1×10^{11}	0.27	14,400	0.0015

2. The force hammer acquisition method is used to measure the radial frequency response function $\mathbf{G_{AA}}$ of the end of the tool holder when the cutter is clamped statically and the radial frequency response function $\mathbf{g_{AA}}$ of the end of the tool holder when the cutter is not clamped. Based on the multiobjective optimization algorithm, the joint surface parameters are identified as follows:

$$G_{AA} = g_{AA} - g_{AA}(g_{AA} + H_{55} + K^{-1})^{-1} g_{AA} \tag{7}$$

where $\mathbf{K}$ is the dynamic parameter matrix of the joint surface. The identification results are summarized in Table 3, where k_{yf} is the deformation–force stiffness; k_{ym} is the deformation–moment stiffness; $k_{\theta f}$ is the turning angle–force stiffness; $k_{\theta m}$ is the turning angle–moment stiffness; and c_{yf} and $c_{\theta m}$ are the force–deformation viscous damping and the torque–turning angle viscous damping, respectively.

Further, $\mathbf{K}$, $\mathbf{g_{AA}}$, and $\mathbf{H_{55}}$ are substituted into Eq. 7. The radial simulation frequency response function of the end of the tool holder when the cutter is clamped statically is calculated, and it is compared with the measured frequency response function. An acceleration sensor is attached on the side of the end of the shank, and the opposite side is struck using a hammer, as shown in Fig. 5. The results are shown in Fig. 6. Figure 6a shows the frequency response of the end of the tool holder in the x direction, and Fig. 6b shows the frequency response in the y direction. The x and y directions are in the same direction as the machine X and Y axes, respectively.

3. According to the frequency response functions $\mathbf{g_{AA}}$, $\mathbf{K}$, $\mathbf{H_{11}}$, $\mathbf{H_{15}}$, $\mathbf{H_{51}}$, and $\mathbf{H_{55}}$ and based on the RCSA method, the tool tip frequency response function $\mathbf{G_{11}}$ of the slender milling cutter can be predicted. The results are shown in Fig. 7. Figure 7a shows the displacement–

Table 3 Dynamic parameters of the interface

	k_{yf}(N/m)	k_{ym} (N • m/m)	$k_{\theta f}$(N/rad)
FRF of the tool tip in the x direction	3.99×10^{9}	5.44×10^{7}	7.33×10^{7}
FRF of the tool tip in the y direction	2.86×10^{9}	8.51×10^{7}	3.38×10^{7}
	$k_{\theta m}$ (N • m/rad)	c_{yf}	$c_{\theta m}$
FRF of the tool tip in the x direction	3.14×10^{6}	0.100	0.031
FRF of the tool tip in the y direction	1.11×10^{6}	0.083	0.023

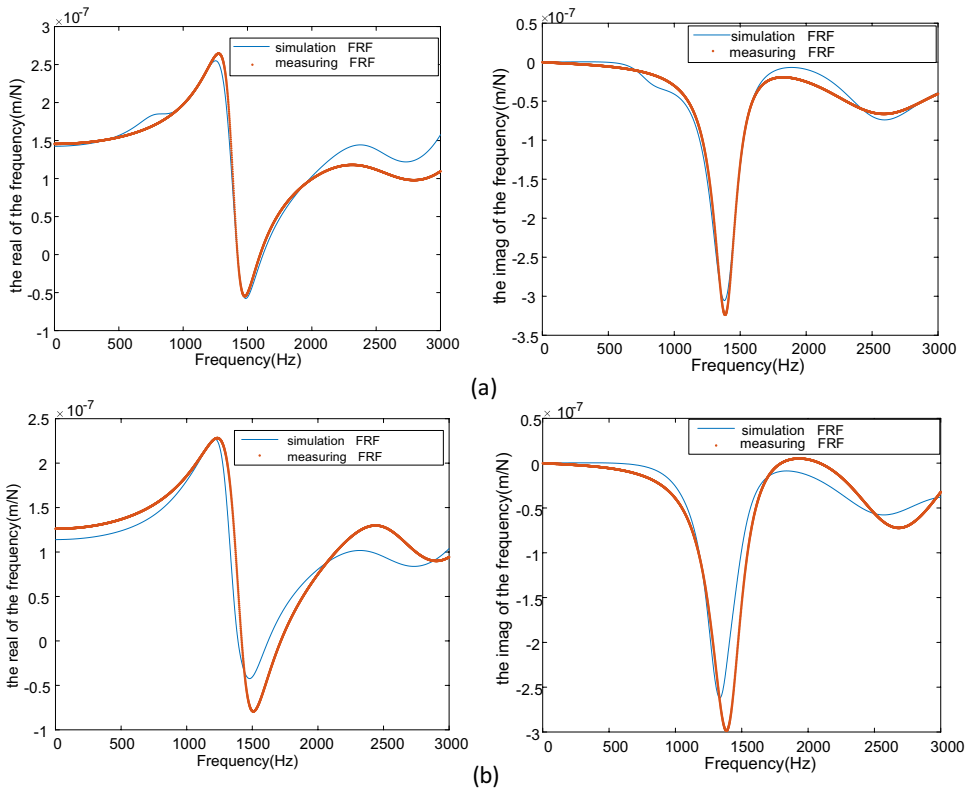

Fig. 6 Comparison of the simulation FRF and measured FRF of the end of the shank

force frequency response function in the x direction of the tool tip, and Fig. 7b shows the displacement–force frequency response function in the y direction of the tool tip. The left panels show the real part of the frequency response function and the right panels show the imaginary part of the frequency response function. In Fig. 7, the tool tip frequency response function is obtained by using a small patch-type acceleration sensor and a force hammer to measure the frequency response function of the 4-mm diameter part of the milling cutter, and calculation is performed using the rigid RCSA method. According to the modal parameters, the time-domain vibration curve is calculated on the basis of the fourth-order Runge–Kutta method.

To realize the multiaxis milling force simulation considering the cutter vibration, first, the milling force without considering the vibration state is discretized into a step force. The step force is substituted into the system state equation to solve the time-domain vibration curve of a milling force cycle. The time-domain vibration curve is superimposed on the machining transition surface to obtain the transition surface topography. Subsequently, the undeformed chip thickness model mentioned in Section 2 is used to predict the cutting force at time t. According to the vibration speed and vibration amount at the previous time and the cutting force at time t, the vibration amount and vibration speed at time t are obtained. The vibration amount is substituted into the tool tip position calculation model at time $t+1$ to obtain the undeformed chip thickness at time $t+1$ and calculate the milling force at time $t+1$. The aforementioned process is repeated until the milling force simulation of the entire flank milling process is completed. The surface gear manufacturing error can be obtained by mapping the cutter vibration at each time to the surface of the face gear along the normal direction.

1.3 Face gear machining path planning

According to the five-axis milling force model of the tangent plane approximation algorithm, to predict the milling force during the five-axis flank milling process of the face gear, it is necessary to calculate the motion coordinates of each axis of the face gear during the machining process. Based on the principle of gear meshing, according to the mathematical model of the involute spur gear profile, the mathematical model of the face gear is established. The profile function of the involute cylindrical gear is expressed as follows:

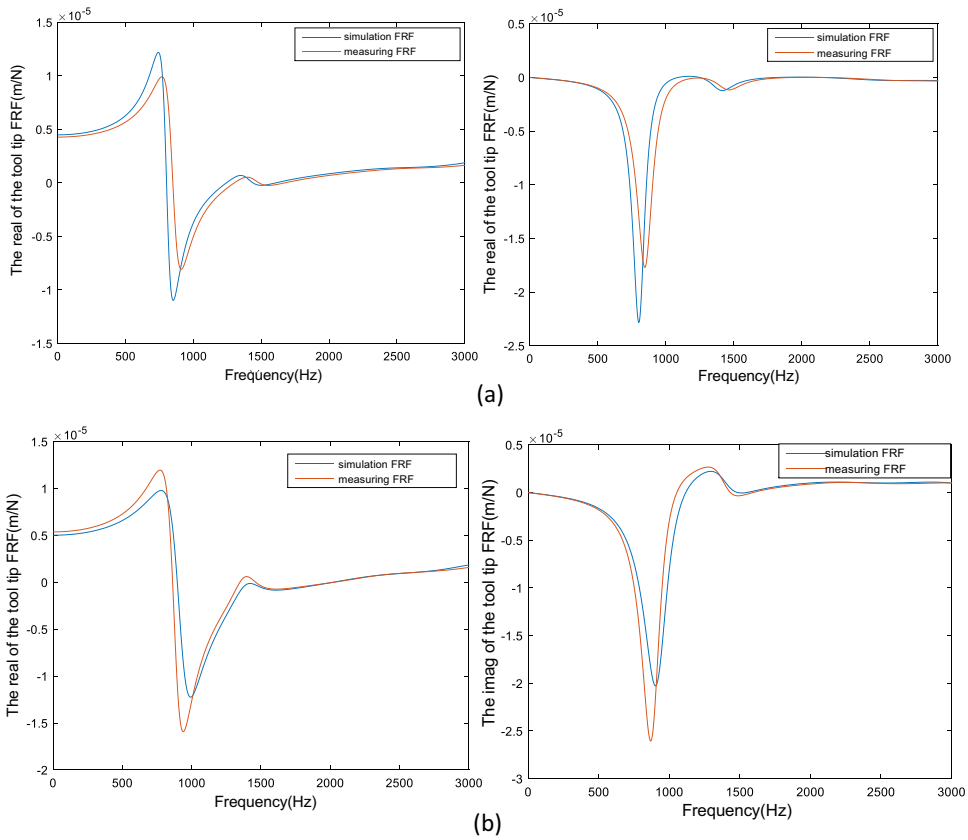

Fig. 7 Comparison of the simulation FRF and measured FRF of the end of the tool tip

$$r_s(\mu_s,\theta_s)=\begin{bmatrix} r_{bs}[sin(\theta_s+\theta_{os})-\theta_s cos(\theta_s+\theta_{os})] \\ -r_{bs}[cos(\theta_s+\theta_{os})+\theta_s sin(\theta_s+\theta_{os})] \\ \mu_s \\ 1 \end{bmatrix} \tag{8}$$

where μ_s and θ_s are the tooth width and spread angle parameters of the gear, respectively; θ_{os} is the initial spread angle parameter of the gear; and r_{bs} is the base circle radius of the gear. The coordinate conversion model of the cylindrical spur gear and face gear is expressed as follows:

$$M_{2s}=\begin{bmatrix} \cos\varphi_2\cos\varphi_s & -\sin\varphi_2\cos\varphi_s & \sin\varphi_s & 0 \\ -\cos\varphi_2\sin\varphi_s & \sin\varphi_2\sin\varphi_s & \cos\varphi_s & 0 \\ -\sin\varphi_2 & -\cos\varphi_2 & 0 & 0 \\ 0 & 0 & 0 & 1 \end{bmatrix} \tag{9}$$

where $\mathbf{M_{2s}}$ is the coordinate transformation between the spur gear coordinate system and the face gear coordinate system, i.e., the matrix, and φ_2 and φ_s are the turning angles of the face gear and the cylindrical spur gear, respectively. According to the principle of gear meshing, the meshing equation between the face gear and the cylindrical spur gear is expressed as follows:

$$\mathrm{f}\left(\theta_s,\varphi_s,u_s\right)=n_s\cdot v=\mathrm{r}_{bs}\text{-}\mathrm{u}_s i_{2s}\cos\varphi_\theta=0 \tag{10}$$

where $\mathbf{n_s}$ is the normal direction of the tooth surface of the pinion gear; $\mathbf{v}$ is the linear velocity direction; μ_s, θ_s, and φ_s are the parameters of the face gear model; f is the meshing equation; and i_{2s} is the transmission ratio. According to Eqs. 9 and 10, the tooth surface equation of the involute face gear can be calculated as follows:

$$\begin{cases} \mathrm{x}_2=r_{bs}[cos\varphi_2((sin\varphi_\theta\mp\theta_s cos\varphi_\theta)-\frac{\sin\varphi_2}{i_{2s}\cos\varphi_\theta})] \\ \mathrm{y}_2=-r_{bs}[sin\varphi_2((sin\varphi_\theta\mp\theta_s cos\varphi_\theta)-\frac{\sin\varphi_2}{i_{2s}\cos\varphi_\theta})] \\ \mathrm{z}_2=-r_{bs}(cos\varphi_\theta\mp\theta_s sin\varphi_\theta) \end{cases} \tag{11}$$

The tooth surface model of the face gear is shown in Fig. 8.

The normal vector of the face gear tooth surface is calculated as follows:

$$n_{r2}=\frac{\partial r_2}{\partial\varphi_s}\times\frac{\partial r_2}{\partial\theta_s} \tag{12}$$

where $\mathbf{n_{r2}}$ is the normal direction of the face gear and $\mathbf{r_2}$ is the tooth surface model of the face gear. Based on the principle of differential geometry, the cutter location point model and the cutter axis vector model are established as follows:

$$r_{2j}^{(i)}=rn_{r2}^{(i)}+r_2^{(i)} \tag{13}$$

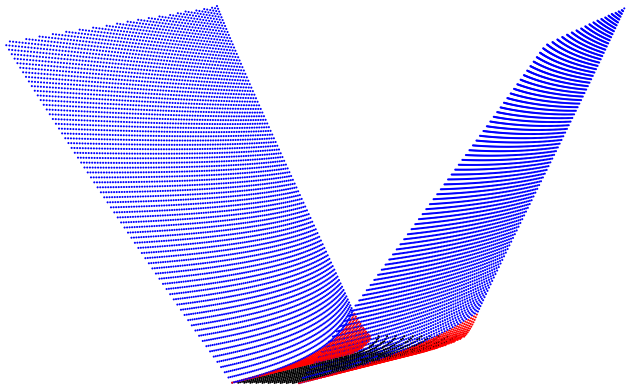

Fig. 8 Face gear model

$$\begin{cases} l_{2j}^{(i)}=n_{r2}^{(i)}\times p_{r2}^{(i)} \\ p_{r2}^{(i)}=r_2^{(i+1)}-r_2^{(i)} \end{cases} \tag{14}$$

where r is the cutter radius; $\mathbf{p_{r2}}$ is the connection direction between the i-th cutter location point and the (i + 1)-th cutter location point; $r_2^{(i)}$ is the coordinate vector of the i-th cutter location point; and $n_{r2}^{(i)}$ is the normal vector of the point on the tooth surface corresponding to the i-th cutter location point.

Table 4 lists the parameters of the face gear. According to the aforementioned models, the cutter location point and cutter path of the face gear are calculated, as shown in Fig. 9. The face gear is finished using the five-axis flank milling method. The machined tooth surface of the face gear is shown in Fig. 10.

1.4 Experimental verification, results, and discussion

Based on the aforementioned theory, the face gear milling process is simulated and compared with the actual measured milling force. As shown in Fig. 11, the face gear milling experiment is performed on the machining center. The face gear is installed on the dynamometer, the dynamometer is installed on the 3R fixture through the adapter plate, and the milling force measurement experiment is conducted on the face gear. During the machining process, the *B* and *C* axes of the machine cutter rotate. Owing to the impact of the gravity of the workpiece and the dynamometer and the inertial force during the rotation, the dynamometer reference will change. Hence, it is necessary to measure the dynamometer data waveform when the machining program is idle and set the measurement data to l_1. The dynamometer measurement data during a section of milling with the same sampling frequency is measured, and the measurement data is set to

Table 4 Parameters of the face gear

Modulus	Face gear tooth number	Cylindrical gear tooth number	Outer diameter of face gear/mm	Inner diameter of face gear/mm	Pressure angle/°	Addendum coefficient	Tip clearance coefficient
3	28	21	47	43	20	1	0.25

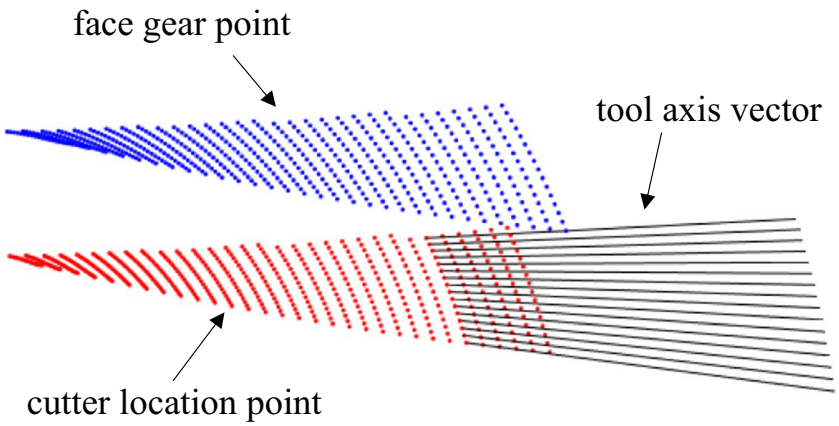

Fig. 9 Cutter path of the face gear

Fig. 10 Face gear based on five-axis side milling

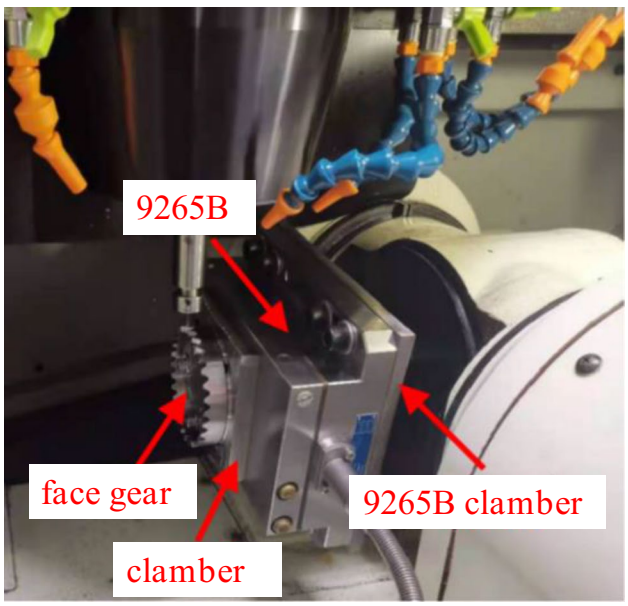

Fig. 11 Cutting force experiment of the Face Gear

l_2. Compared with the amplitude of the milling force, as the change in the center of gravity position of the workpiece and the dynamometer has a significant impact on the reading of the dynamometer, the amplitude of the milling force is within 1 N, while the amplitude of the influence of gravity is around 15 N. The l_1 waveform is regarded as a dynamometer reference during machining to obtain the milling force. The measurement data when the processing code is executed is intercepted in l_1, and the measurement data of equal duration is intercepted in l_2. Then, the standard deviation of the l_1 and l_2 intercepted data sampling points is calculated in a one-to-one correspondence in order. When the sum of the standard deviations of all the sampling points reaches the minimum value, the intercepted measurement data of l_2 is considered

to be synchronized with the processing code executed by the measurement data l_1. At this time, the l_1 data is subtracted from the l_2 intercepted data, and the obtained data is the multiaxis machining milling force measurement data in the face gear coordinate system.

A 2-mm milling cutter is used to mill the face gear, and the exposed length of the milling cutter is the same as that in Sect. 2. When milling the tooth surface of the face gear, the rotation speed is 10000 r/min, the feed rate is 1200 mm/min, and the tooth length of the face gear is around 4 mm. The tooth surface is divided into 80 tooth profiles for milling, and the milling force is simulated. Combined with the transient milling force coefficient identification method, the milling force coefficient is calculated as shown in Table 5. By integrating the contents of Section 2, the milling force in the face gear milling process is predicted. Figure 12 shows the variation of the rotation angle of the B and C axes. The B axis rotates in the negative direction of each cutting path, whereas the C axis rotates in the positive direction of each cutting path. Figure 13a shows the milling force of the 2nd tooth profile, Fig. 13b shows the milling force of the 20th tooth profile, and Fig. 13c shows the milling force of the 40th tooth profile. Each group of milling force simulation and measurement comparison figures from left to right are the x direction milling force in the face gear–workpiece coordinate system, the y direction milling force in the face gear–workpiece coordinate system, and the z direction milling force in the face gear–workpiece coordinate system. The blue curve is the experiment curve, and the red curve is the simulation curve. The amplitude and trend of the experimental milling force curve and the simulation milling force curve are consistent, and the maximum amplitude error does not exceed 0.2 N. Because of the influence of the rotation angles of the B and C axes, the cutting force along the x axis first decreases and then increases. The cutting force along the y axis decreases progressively, whereas the cutting force along the z axis increases progressively. However, some errors persist for the following reasons.

1. The initial phase angle of the simulated milling cutter is different from the initial phase angle of the milling cutter in the actual milling process. As the initial phase angle cannot be measured in the actual milling process, there is a certain error in the phase between the actual milling force and the simulated milling force.
2. The existing noise when the dynamometer is used to measure the milling force affects the accuracy of the experimental milling force.
3. There is a certain error between the surface morphology of the blank during actual roughing and the surface morphology of the blank when the milling force is calculated. This affects the calculation of the cut-in and cut-out angles of the milling cutter, which influences the milling force.

Table 5 Cutting force coefficient

	K_{tc}	K_{te}	K_{rc}
Cutting force coefficient	6841.7	15.1	5435.2
	K_{re}	K_{ac}	K_{ae}
Cutting force coefficient	19.6	1560.1	13.3

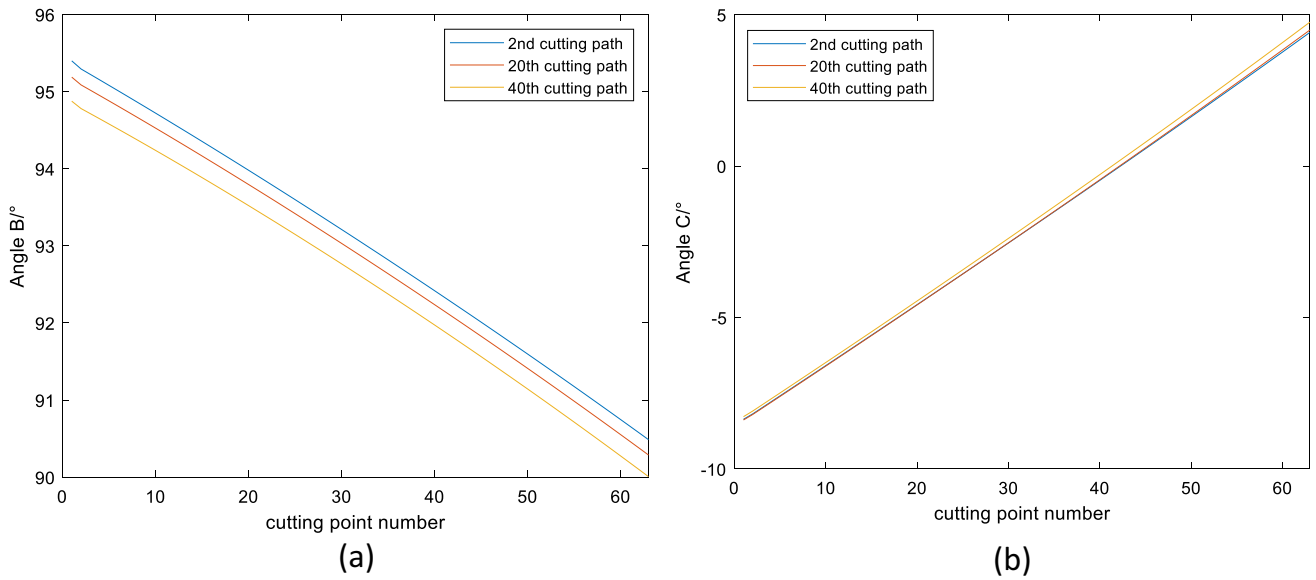

Fig. 12 Variation of the rotation angles of the B and C axes of the machining center

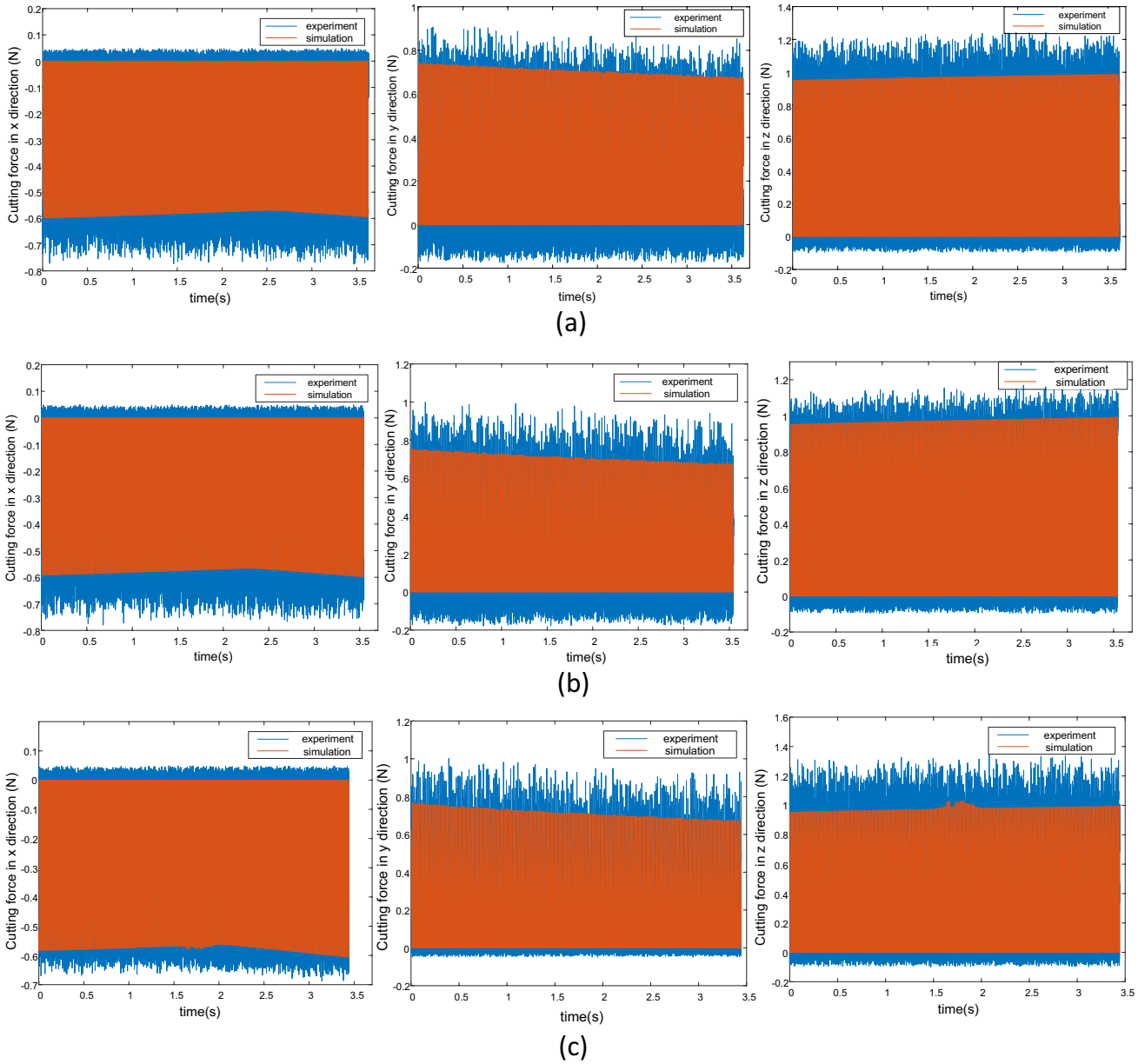

Fig. 13 Comparison of the simulation cutting force and measured cutting force

By integrating the frequency response of the tool tip, the milling force and vibration during the milling process are predicted. The results of cutter vibration are shown in Fig. 12. Figure 12a shows the vibration curve of the cutter in the *x* direction, and Fig. 12b shows the vibration curve of the cutter in the *y* direction. One cycle of the milling force under coupled vibration is compared with one cycle of the milling force under uncoupled vibration. As shown in Fig. 14, cutting vibration does not have a significant effect on the milling force curve. As the vibration of the tool tip is only 3–4 μm and the radial depth of cut in milling is 0.1 mm, the vibration does not have a significant effect on the cut-in and cut-out angles. Furthermore, owing to the small change in the normal direction of the tooth surface of the face gear, the amplitude and waveform of the milling force in adjacent cycles are basically the same, and the vibration waveforms in adjacent cycles are also basically the same. As the vibration waveform characteristics mapped on the transition surface in the actual cutting process are not significantly different from the vibration waveform characteristics coupled to the milling

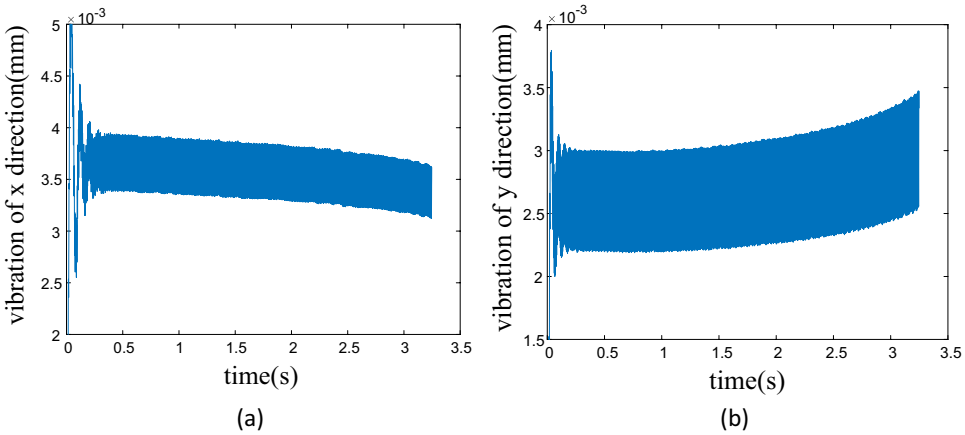

Fig. 14 Vibration of the tool tip

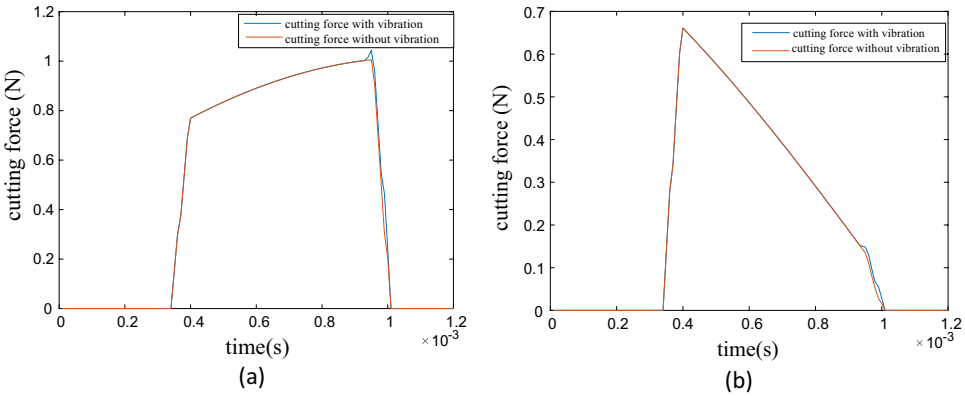

Fig. 15 Comparison of the cutting force including the tool tip vibration and the cutting force without vibration

path, the vibration does not have a significant impact on the undeformed chip thickness.

The cutter vibration does not have a significant effect on the milling force with a small amplitude, as shown in Fig. 15. However, in the case of a large depth of cut and single tooth feed, owing to the large amplitude of the milling force, the cutter vibration caused by the large amplitude is large, and its impact on the undeformed chip thickness is also significant. Hence, the influence of the cutter vibration on the milling force is relatively obvious [17]. Furthermore, it is necessary to use the dynamic milling force simulation method considering the dynamic characteristics of the tool tip in order to predict the milling force.

Based on the tool tip vibration and the tool path, the machining error can be solved by mapping the vibration to the face gear surface. Figure 16 shows the machining error simulation results, and Fig. 17 shows the face gear error measuring process. The measured results are summarized in Table 6. The simulated and measured results are in the range of 3–5 μm. Some errors persist between the simulated results and the measured results. Because the machining

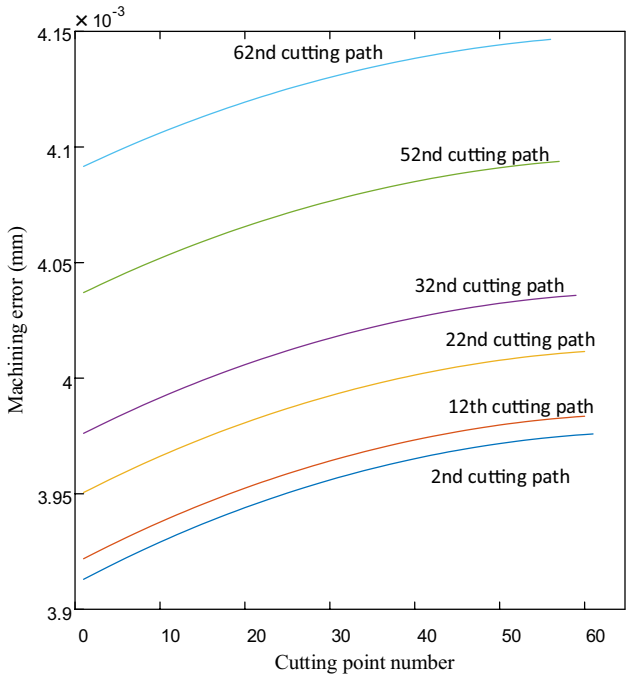

Fig. 16 Machining error prediction results of the face gear

Fig. 17 Machining error measuring process of the face gear

error model in this study only considers the deformation of the cutter, the transient vibration of the cutter is ignored.

2 Conclusion

To realize high-precision manufacturing of face gears with a universal milling machine, this study proposed a slender milling cutter for flank milling finishing of face gears. Based on the RCSA method, the frequency response function of the milling tool tip of the machining system was measured indirectly. Moreover, the milling force model of the sculptured surface flank milling process with coupled vibration was established. This model was used to simulate the milling force of face gear machining. The milling force obtained by the actual measurement was experimentally verified to be consistent with the trend of the simulated milling force, and the maximum error between the simulated milling force and the actual milling force did not exceed 0.2 N. In addition, the tool tip vibration and tooth surface machining error during the five-axis flank milling of the face gear were predicted. The proposed model has the following advantages:

1. It can accurately predict the tool tip frequency response function using the RCSA. Moreover, it overcomes the difficulty in measuring the tool tip frequency response function [22].
2. It can predict the sculptured surface machining error considering the interaction of the cutting force and the machining system, which improves the precision of the machining error prediction result [17].

Certain aspects of the tool tip frequency response function modeling method and the dynamic milling force model used in this study require improvement, such as the impact of the milling cutter wear on the milling force, the impact of the centrifugal force generated by the spindle mass eccentricity and the milling force on the dynamic parameters of the joint surface, and the impact of the cutting heat on the cutting characteristics of the material.

Table 6 Measured machining error

Coordinates/mm	Deviation/mm	Position
(2.1399, 43.9526, – 2.4829)	0.0058	Middle of the surface
(2.7782, 44.7744, – 3.7594)	0.0032	Middle of the surface
(2.6888, 45.3542, – 3.6012)	0.0022	Middle of the surface
(2.3172, 44.4290, – 2.8728)	0.0049	Middle of the surface
(2.3494, 45.1424, – 2.9811)	0.003	Middle of the surface
(3.0460, – 44.0437, – 4.3177)	0.0024	Bottom of the surface
(1.0947, – 44.1864, – 0.3375)	0.0038	Top of the surface
(– 43.2065, – 13.2291, – 4.6373)	0.0028	Bottom of the surface
(– 42.4944, – 11.9728, – 2.6511)	0.0035	Middle of the surface
(– 43.2728, – 13.2291, – 4.6373)	0.0032	Bottom of the surface
(– 44.2256, – 12.4009, – 2.8679)	0.0037	Middle of the surface
(– 43.3718, – 7.0027, – 3.8887)	0.0026	Middle of the surface
(3.0478, 44.2820, – 4.2971)	0.0061	Bottom of the surface
(3.2251, 45.2712, – 4.5511)	0.0035	Bottom of the surface
(3.4913, 45.5341, – 4.9959)	0.0056	Bottom of the surface

Author's contributions Sijie Cai established the cutting force mathematical model, the dynamics mathematical model, and the cutting path mathematical model and wrote the codes of these algorithms. Jianchun Liu, Zhiqin Cai, and Bin Yao designed the experiments of the cutting force measurement and the face gear tooth surface errors measurement. Haipeng Huang, Bingjing Lin, Jianchun Lin, and Haibin Huang proposed the fund of the face gear machining and measuring experiments.

Funding This work was financially supported by the National Natural Science Foundation of China (No. 51905459, Zhiqin Cai), the Natural Science Foundation of Fujian Province (No. 2020J01274, Binjing Lin), and the STS Science and Technology Foundation of Fujian Province (No. 2021T3069, Haipeng Huang).

Data availability All data generated during this study are included in this published article.

Code availability Some parts of the code about the mathematical model during the current study are available from the corresponding author on reasonable request.

Declarations

Ethics approval Not applicable.

Consent to participate Sijie Cai, Jianchun Liu, Bin Yao, Zhiqin Cai, Zhihuang Shen, Haipeng Huang, Bingjing Lin, Jianchun Lin, and Haibin Huang are willing to be listed as the authors of this essay. We further confirm that all authors have checked the manuscript.

Consent for publication We further confirm that all authors have checked the manuscript and have agreed to the publication.

Competing interests The authors no competing interests.

References

1. Brecher C, Esser M, Witt S (2009) Interaction of manufacturing process and machine cutter. Cirp Annals Manuf Technol 58(2):588–607
2. Chen W, Huo D, Xie W et al (2016) Integrated simulation method for interaction between manufacturing process and machine cutter. Chin J Mech Eng 29(6):1090–1095
3. Kline W, De Vor R, Lindberg J (1982) The prediction of cutting forces in end milling with application to cornering cuts. Int J Mach Cutter Design Res 22(1):7–22
4. Altintas Y, Spence A (1991) End milling force algorithms for CAD systems. CIRP Ann-Manuf Technol 40(1):31–34
5. Ko J, Yun W, Cho D et al (2002) Development of a virtual machining system, part 1: approximation of the size effect for cutting force prediction. Int J Mach Cutters Manuf 42:1595–1605
6. Tuysuz O, Altintas Y, Feng HY (2013) Prediction of cutting forces in three and five-axis ball-end milling with cutter indentation effect. Int J Mach Cutters Manuf 66:66–81
7. Cao Q, Zhao J, Li Y (2011) Cutting force modelling considering cutter deflection for sculptured surface milling. Int J Manuf Technol Manage 22(4):362–375
8. Zhang X, Zhang J, Pang B et al (2016) An accurate prediction method of cutting forces in 5-axis flank milling of sculptured surface. Int J Mach Cutters Manuf 104:26–36
9. Rao V, Rao P (2005) Modelling of tooth path and process geometry in peripheral milling of curved surfaces. Int J Mach Cutters Manuf 45(6):617–630
10. Kim GM, Cho PJ, Chu CN (2000) Cutting force prediction of sculptured surface ball-end milling using Z-map. Int J Mach Cutters Manuf 40(2):277–291
11. Yao Q, Wu B, Luo M et al (2018) On-line cutting force coefficients identification for bull-end milling process with vibration. Measurement 125:243–253
12. Yao Q, Luo M, Zhang D et al (2018) Identification of cutting force coefficients in machining process considering cutter vibration. Mech Syst Signal Process 103:39–59
13. Schmitz TL, Powell K, Won D et al (2007) Shrink fit tool holder connection stiffness/damping modeling for frequency response prediction in milling. Int J Mach Cutters Manuf 47(9):1368–1380
14. Schmitz TL, Duncan GS (2005) Three-component receptance coupling substructure analysis for cutter point dynamics prediction. J Manuf Sci Eng 127(4):781–790
15. Yokoyama T (1990) Vibrations of a hanging Timoshenko beam under gravity. J Sound Vib 141(2):245–258
16. Wei F, Yao B, Yu X et al (2016) Simulation of grinding process for cemented carbide based on an integrated process-machine model. Int J Adv Manuf Technol 89(1–4):1–8
17. Cai S, Yao B, Feng W et al (2020) Milling process simulation for the variable pitch cutter based on an integrated process-machine model. Int J Adv Manuf Technol 106:2779–2791
18. Altintas Y, Tuysuz O, Habibi M (2018) Virtual compensation of deflection errors in 5-axis ball end milling of turbine blades. J Manuf Sci Eng 141(3):365–368
19. Li ZL, Tuysuz O, Zhu LM et al (2018) Surface form error prediction in five-axis flank milling of thin-walled parts. Int J Mach Cutters Manuf 128:21–32
20. Li XP, Zheng HQ, Wong YS et al (2000) An approach to theoretical modeling and simulation of face milling forces. J Manuf Process 2(4):225–240
21. Rivière-Lorphèvre Edouard E (2009) Filippi. Mechanistic cutting force model parameters evaluation in milling taking cutter radial runout into account. Int J Adv Manuf Technol 45(1–2):8–15
22. Malekian M, Park SS, Jun M (2009) Modeling of dynamic micro-milling cutting forces. Int J Mach Cutters Manuf 49(7–8):586–598